Preprint
UCRL-JC-139454

An Experimental Testbed For The Study Of Hydrodynamic Issues In Supernovae

H. F. Robey, J. O. Kane, B. A. Remington, R. P. Drake, O. A. Hurricane, H. Louis, R. J. Wallace, J. Knauer, P. Keiter, D. Arnett, D. D. Ryutov

This article was submitted to
42nd Annual Meeting of the American Physical Society Division of Plasma Physics
Quebec, Canada
October 23-27, 2000

U.S. Department of Energy

Lawrence Livermore National Laboratory

October 9, 2000

An experimental testbed for the study of hydrodynamic issues in supernovae

H. F. Robey[1], J. O. Kane[1], B. A. Remington[1], R. P. Drake[2], O. A. Hurricane[1], H. Louis[1], R. J. Wallace[1], J. Knauer[3], P. Keiter[2], D. Arnett[4], D. D. Ryutov[1]

[1]Inertial Confinement Fusion Program, Lawrence Livermore National Laboratory

Livermore, California 94550

[1]Atmospheric, Oceanic, and Space Sciences, University of Michigan,

Ann Arbor, MI 48105

[3]Laboratory for Laser Energetics, University of Rochester

Rochester, NY 14623

[4]University of Arizona, Tucson, AZ

October 9, 2000

Prepared for submission to

Physics of Plasmas

ABSTRACT

More than a decade after the explosion of SN 1987A, unresolved discrepancies still remain in attempts to numerically simulate the mixing processes initiated by the passage of a very strong shock through the layered structure of the progenitor star. Numerically computed velocities of the radioactive ^{56}Ni & ^{56}Co, produced by shock-induced explosive burning within the silicon layer for example, are still more than 50% too low as compared with the measured velocities. In order to resolve such discrepancies between observation and simulation, an experimental testbed has been designed on the Omega Laser for the study of hydrodynamic issues of importance to supernovae (SNe). In this paper, we present results from a series of scaled laboratory experiments designed to isolate and explore several issues in the hydrodynamics of SN explosions. The results of the experiments are compared with numerical simulations and are generally found to be in reasonable agreement.

1. INTRODUCTION

In February of 1987, a spectacular burst of light from SN 1987A was first observed, subsequently generating an enormous wealth of observational data on this phenomenon. These observations strongly suggested that extensive mixing of the inner layers into the outer layers of the progenitor star had occurred. This material mixing, due to the Rayleigh-Taylor[1-2] (RT) and Richtmyer-Meshkov[3-4] (RM) instabilities, was indicated by several forms of observation. X-ray emission from ^{56}Ni and ^{56}Co, generated in the shock-induced explosive burning within the silicon layer, was observed at about 6 months[5], whereas one-dimensional spherically symmetrical numerical simulations predicted observation at approximately one year[6-7]. The peak velocities of the ^{56}Co were observed to be well in excess of 3000 km/sec[8-10]. Early two-dimensional numerical simulations, by comparison,

produced peak velocities less than 2000 km/sec[11-15]. More recent 2D simulations[16], beginning just after core bounce, find initially very large velocities (up to 4000 km/sec) of the newly created Fe group elements. After impact with the reverse shock at the He-H interface, however, the velocities are again decelerated to a value near 2000 km/sec. Thus, the discrepancy between observation and simulation persists.

A number of possible explanations for these discrepancies are under active exploration. More detailed 2D simulations of the pre-existing convectively driven structure at the edge of the oxygen layer[17-19] have been performed to better quantify the level of the initial perturbation. The mixing resulting from shock propagation through this layer, however, was still found insufficient to explain the observations. Three-dimensional effects are known from theoretical, numerical, and experimental work to increase the mixing over 2D perturbations[20-23]. Initial 3D simulations of the SN mixing problem[24-25], however, still underpredict the material velocities.

Two possibilities exist for resolving this problem. The first possibility is that the assumptions underlying previous numerical simulations are incorrect or contain incomplete physics. An example is the recent work of Khokhlov et al.[26] that brings the additional effects of rotation and magnetic fields into the problem. The resulting collapse launches a highly asymmetric explosion with bipolar jets and the formation of bow shocks and Mach disks and demonstrates that the assumption of spherical symmetry may be incorrect. The second possibility is that existing computer models may be incorrectly calculating the hydrodynamic evolution of the system. All numerical methods necessarily include approximations in the underlying equations. Different schemes use different orders of accuracy, employ non-physical artificial viscosities to assure stability of the calculations, and in spherical geometry can suffer from vanishing metrics[16, 25] and grid-induced numerical instability[16, 27]. Numerical results often agree at the largest scales of motion, but can differ strongly at smaller scales (see for example, ref 28). In an effort to address this second

possibility, laboratory experiments have been initiated[29-33] to provide a set of benchmark data with which to validate the performance of astrophysical codes.

The purpose of the present paper is twofold. The first goal is to establish the range of astrophysical phenomena that can be addressed on a laser facility. To that end, we present initial results from a series of scaled laboratory experiments designed to isolate and explore four separate issues of relevance to the SN mixing problem. The first experiment explores the effects of spherical divergence on the instability evolution. The second studies the possibility of coupling between two spatially separated interfaces. The third compares and quantifies the difference between instability growth in two and three dimensions. And the fourth begins to look at the evolution of an interface of more complicated modal content. The second goal of this work is to serve as a first rough assessment of the validity of numerical codes used for astrophysics. For each experiment, comparisons are made with numerical simulation, and the implications and relevance to the SN problem are assessed.

II. SCALING ISSUES

Conner and Taylor[34], and more recently Ryutov et al.[35], have presented general scaling relations that govern the validity of experiments intended to replicate the hydrodynamic phenomena occurring in astrophysical systems. In this section, we apply those scaling relations to the first of the problems that we will examine experimentally, that of the effect of spherical divergence on instability evolution in the explosion phase of supernovae (SNe). Specifically, the emphasis is placed on studying the instability evolution at the He / H interface.

The details of the experiment will be described in detail in section IV. For discussion of scaling issues, we simply note the essential elements of the experimental setup. The more dense He layer in the SN progenitor is simulated in the experiment with a hemispherical shell of polystyrene (CH) with a density $\rho = 1.37$ g/cm^3. The surrounding H layer is simulated with a low density (ρ=0.1 g/cm^3) carbon foam. In the Omega experiment,

a strong shock is driven through the interface between these two materials by laser radiation. Passage of this shock through the interface initially accelerates the interface generating Richtmyer-Meshkov instability. The interface is then subsequently decelerated by the surrounding H (foam) envelope. Figure 1(a) shows the velocity history of both the SN He-H interface as computed using the astrophysical code PROMETHEUS[5] and the laboratory CH-foam interface computed using the one-dimensional radiation-hydrodynamics code HYADES[36]. As is seen, the temporal evolution of both systems is quite similar. The corresponding spatial structure in the vicinity of the interface is shown in Figure 1(b) for both the density and pressure fields. The spatial structure is shown for the SN at t = 2000 sec and for the corresponding scaled Omega experiment at t = 20 ns. In both cases, the outward propagating shock is off to the right of the Figure. The spatial similarity, near the interface, between the two vastly disparate scales is again readily apparent. This spatial similarity is only local, however, and farther from the interface, the two systems will differ.

Table I shows the comparison between the physical scales involved in the SN and the laboratory experiment. The characteristic length scale differs by 14 orders of magnitude, and the pressure, density, temperature, and ionization state show considerable differences as well. Table II gives several of the important derived parameters that quantify the degree of scaled similarity and the applicability of the Euler equations to these two problems. The first parameter $v / (p/\rho)^{1/2}$, which has the form of a Mach number, establishes the degree to which the two systems will exhibit similar behavior[35]. For both systems, this parameter is nearly equal. If the boundary conditions were also identical for these two systems, then they would indeed evolve identically. In fact, the boundary conditions for this experiment are not identical. The important difference being that the density profile in the SN progenitor falls off radially whereas in the experiment the density is constant. This breaks the direct similarity with the astrophysical situation, but the experiment still provides useful data against which codes can be compared.

The applicability of the Euler equations is quantified by demonstrating that dissipative processes such as viscosity, thermal conductivity, and radiative transport are small in comparison with the inertial terms in the equations of motion (Table II). These processes are quantified by the appropriate non-dimensional parameters: the Reynolds number, Peclet number, and radiation Peclet number. All these were discussed by Ryutov et al.[35]. In that work, the viscosity and thermal conductivity were estimated using simple analytical formulae of Braginski[37] applicable to the high temperature, low density plasmas characteristic of SN. For the laboratory plasma, however, the temperature can be much lower and the density considerably higher than that in the SN (see Table I). In this case, the plasma ions are no longer necessarily weakly coupled, and the kinetic theory approach of Braginski is not always appropriate. For such dense plasma conditions, we use an improved model for both the thermal conductivity[38] and the kinematic viscosity[39], both of which are applicable over a broad range of temperature and density.

One sees in Table II that the Reynolds number, the Peclet number, and the radiation Peclet number are all large for the SN as well as for the Omega experiment. This indicates that for the large-scale features of interest (shock and interface positions, growth of perturbations of wavelength comparable to the system size, etc.), the Euler equations apply, and that viscous, thermal, and radiation effects can be neglected. At a sufficiently small spatial scale, which will be a small fraction of the system size (and well below the diagnostic resolution of the present experiments), these effects may no longer be negligible. On that scale, as previously discussed[35], dissipation will affect the structure of the resulting turbulence.

III. CONFIGURATION OF THE EXPERIMENTAL TESTBED

The experiments are conducted on the Omega Laser at the Laboratory for Laser Energetics (LLE), Univ. of Rochester[40-43]. In order to facilitate the timely execution of several different experiments on the Omega laser, it was important that all of the

experiments have as common an experimental configuration as possible. Figure 2 shows an illustration of the generic experimental setup used for all of the Omega experiments. The target package differs from experiment to experiment, the specific details of which will be given in Section IV.

The strong shock conditions of interest are achieved by directing either 6 beams (divergent experiment) or 10 beams (all other experiments) with a nominal measured energy of 420-500 J / beam (again experiment dependent) at a laser wavelength of 0.351μm onto the target. Each beam has a super-Gaussian spatial intensity profile. The combined spatial profile of the drive beams is well represented by the intensity profile $I / I_0 = \exp[-(r / 412\mu m)]^{4.7}$, with $I_o = 2\text{-}5 \times 10^{14}$ W/cm^2. The intensity of this profile is reasonably constant over a central diameter of 600 μm, and falls off by about 10% by 800 μm. The typical diameter of the targets, by comparison, is 800 μm. Since considerable laser energy extends laterally beyond the diameter of the target packages, a shield (either Au or Be) with an outer diameter 2.5-mm diameter and an inner aperture of 440 μm (divergent) or 950 μm (planar) was used to delay the propagation of a shock around the sides of the target. This proved to be successful in generating both spherical shock propagation through a hemispherical capsule as well as planar shock propagation for the planar targets. For all experiments, the temporal pulse is nominally flat with a duration of 1 ns.

The inner 6 drive beams, forming an angle of 23.2° from the target normal in a hexagonal pattern, were overlapped at the target center. An additional four beams at an angle of 47.8° from the target normal were also overlapped at the target center. These beams occupy 4 corners of a hexagonal pattern. The remaining two beams which complete the outer beam cone at 47.8° are driven by a different amplifier (Omega Leg II) which is delayed in time by 10–100 ns relative to the drive beams for our experiments. Beams from this amplifier are used for backlighting the target, and are therefore not available for the drive.

The evolution of the instability at the interfaces within the targets was diagnosed with x-rays generated by directing an additional 7 Omega beams onto a thin backlighter foil located 4 mm from the center of the target as shown in Figure 2. These beams, driven by a separate oscillator, were delayed in time relative to the drive beams by up to 100 ns to observe the instability evolution at late times. The contrast generated by differential absorption of the backlighter x-rays by the target materials was imaged with a gated framing camera[44]. Many of the experiments also contained an additional backlighter (not shown in Figure 2) oriented in an orthogonal direction to enable simultaneous face-on imaging of the interface evolution. An additional six delayed beams were directed onto this backlighter as well, and the resulting x-ray absorption along the axis of the target was imaged on a second gated x-ray framing camera. The results of the face-on measurements will not be discussed here.

4. EXPERIMENTAL RESULTS

A.) The effect of spherical divergence

In order to investigate the effect of spherical divergence on the evolution of instability at an interface, we use targets consisting of a hemispherical shell of 3% Ge-doped polystyrene (CH) with a density $\rho = 1.37$ g/cm^3 surrounded by a volume of lower density foam. The capsule ID is nominally 440 μm, and the OD = 650 μm, giving a shell thickness of approximately 110 μm. The capsule is embedded within a cylinder of carbonized resorcinol formaldehyde (CRF), a porous foam with density $\rho = 0.1$ g/cm^3. The CRF cylinder measures 1500 μm in diameter by 1500 μm in length. An initial "two-dimensional" perturbation is imposed on the outer surface of the CH(Ge) capsule. The perturbation, produced by laser ablation, has a wavelength $\lambda = 70$ μm and a peak-to-valley amplitude of $a_{p/v} = 10$ μm. The ripples form parallel grooves in the outer CH(Ge) surface with the crests aligned parallel with the diagnostic line of sight. Five cycles of the perturbation are included covering a projected square area of 350 μm x 350 μm on the

hemispherical surface. Figure 3(a) shows an illustration of the geometry of the perturbed hemisphere. This geometry provides a clear, well-defined side-on view of the ripple amplitude for back illuminated radiography. The disadvantage is that the perturbation is fully three-dimensional with two-dimensional ripples imposed on a spherical surface and is therefore difficult to simulate numerically.

Figure 3 shows experimental radiographs of the instability evolution obtained with a Sc backlighter foil generating 2.8 keV He-α x-rays. In Figure 3(b), an unperturbed capsule is shown at t = 13.6 μs as a reference case. The experiment magnification is fairly low (4x) in order to obtain a large enough field of view to observe the shape of the entire expanding capsule. The capsule shell is seen to remain intact with no evidence of instability growth, indicating that the laser drive is sufficiently uniform. By comparison with the initial capsule position, the shell radius has expanded to $R / R_0 = 2.7$, and the capsule thickness has decreased to approximately half of its initial value. The expanded capsule shape is seen to be very nearly spherical as well. The shock is also seen in the image just outside of the expanding shell.

Figure 3(c) shows the corresponding image at the same time, t = 13.6 μs, for a capsule with a λ = 70 μm and nominal $a_{P/V}$ = 10 μm perturbation. Again, the radial divergence factor is 2.7. The wavelength of the perturbation grows by an identical factor. These two features, the capsule thinning and the increase in perturbation wavelength, are two essential features that differentiate the instability evolution in spherically divergent geometry from that which is observed in the much more extensively studied case of planar geometry.

Figure 3(d) shows the continued evolution of the instability at t = 26 ns. The overall capsule shape remains reasonably spherical with a spherical divergence factor now increased to 3.4. From Figures 3(c & d) the shock position, which is very close to that of the interface, is seen to correspond almost exactly to that of a spherically expanding Taylor-Sedov blast wave with $R_{26} / R_{13} = (t_{26} / t_{13})^{2/5}$. The amplitude of the perturbation is difficult

to measure in Figure 3(c) since the capsule has completely broken up, with all of the more dense capsule material appearing in the spikes which lay very close to the shock front.

A higher resolution view (8x magnification) of the interface t = 13 ns is shown in Figure 3(e). At this magnification, one can now clearly see the full extent of the perturbation and its proximity to the shock. The shape of the perturbed interface shows rather broad bubbles and spikes, more characteristic of a much lower Atwood number flow. The reason for this is attributed to the proximity of the shock, which acts effectively acts as a rigid boundary suppressing the growth of the CH(Ge) spikes relative to the growth of the foam bubbles. This result can be compared with an equivalent planar interface as shown in Figure 3(f), where a 108 μm thick planar layer of 4.3% Br-doped CH was accelerated with a nominally identical drive into the same 0.1 g/cm^3 CRF. Though the observation time is the same in Figures 3(e & f), several distinct differences are observed between the spherically diverging and the planar cases. The wavelength remains much closer to the initially imposed wavelength in the planar case, although there is still some divergence due to shock diffraction effects. The shape of the spikes is also observed to be significantly more elongated with more pronounced "mushroom caps". The shock in this case is seen to be somewhat further from the interface as well.

Numerical simulations of this experiment were performed with a 2D Arbitrary Lagrangian-Eulerian radiation-hydrodynamics code (CALE[45]). Since an extensive discussion of the numerical simulation of these experiments is given in Drake et al.[46] for the divergent experiments and Kane et al.[47] for the planar experiments, we confine our discussion here to the results of the simulations. Figure 3 shows a plot of the amplitude of the perturbation for t = 13 ns and 18 ns for both the spherically diverging and the planar experiments. The later time data of t = 26ns is not included in this Figure, since the capsule shell has completely broken up and the amplitude cannot be measured. The result of the 2D numerical simulation is shown as well. Since the shock velocity remains more constant in the planar case, the distance traveled by the interfaces differs between the divergent and

planar experiments. For this reason, the amplitude of the perturbation is plotted as a function of the distance traveled by the interface. For comparable values of the distance traveled, the planar case is seen to grow by nearly a factor of two more than the divergent case. The numerical simulations show generally good agreement with the data. The disagreement with the data is most likely a result of the difficulty measuring the amplitude of the perturbation as the diagnostic is measuring the integrated absorption of the Sc x-rays through a two-dimensional perturbation imposed on a spherical interface.

B.) Coupling between interfaces

The second experiment considers the possible coupling between spatially separated interfaces. Coupling can occur either by the impact of structure from a previous interface[25], or as is investigated here, by the propagation of a perturbed shock originating from the passage through a previously perturbed interface.

Figure 4(a) shows an exploded view of the target used for the experiments. In order to approximate the decreasing radial density profile of a star, a target is prepared which consists of a series of layers of decreasing density mounted within a Be shock tube. The presence of the shock tube improves the planarity of the experiment by decreasing the lateral expansion of the target materials. The shock tube has an OD of 1100 μm and an ID of 800 μm. Beginning at the laser drive end, the target consists of a 10 μm polystyrene ablator layer (ρ = 1.05 g/cm^3) followed by a 90 μm Cu layer (ρ = 8.9 g/cm^3), a 150 μm polyimide layer (ρ = 1.41 g/cm^3), with the remainder of the target filled with a low density CRF foam (ρ = 0.1 g/cm^3). Embedded within the polyimide layer is a radiographically opaque tracer strip of 4.3% brominated polystyrene. The tracer layer measures 75 μm in the direction along the Be tube, and is 200 μm wide along the diagnostic line-of-sight direction. The density of this CH(Br) layer (ρ = 1.42 g/cm^3) is nearly identical to that of the surrounding polyimide. When viewed in side-illuminated radiography, nearly all of the contrast comes from this opaque tracer layer, allowing visualization of the shock-imprinted

structure at interface 2 over only the central 200 μm of the target. This helps to eliminate wall effects that are inherent in such an integrated line-of-sight diagnostic. A perturbation of wavelength λ = 200 μm and amplitude $a_{p/v}$ = 30 μm is pre-imposed at the Cu-polyimide interface. The perturbation at this interface grows due to Rayleigh-Taylor and Richtmyer-Meshkov instabilities, but the focus of this experiment is on the possibility of imprinting a perturbation at the second initially unperturbed interface.

The target is driven by 10 beams of the Omega laser with a measured average energy of 420 J / beam in a 1 ns pulse at a laser wavelength of 0.351μm. For 10 beams overlapped at target chamber center, the peak intensity is 8.9 x 10^{14} W/cm^2. A 75 μm thick, 2.5 mm diameter Beryllium shield with a central aperture of 950 μm diameter is mounted at the front of the target. The average intensity incident on the CH ablator over this central aperture is 5.7 x 10^{14} W/cm^2.

The evolution of both the instability at the Cu / polyimide interface and the shock-imprinted perturbation at the CH(Br) / CRF interface were diagnosed with 6.7 keV x-rays from a 12 μm thick Fe backlighter foil located 4 mm from the center of the target. These beams were delayed in time relative to the drive beams by up to 91 ns to observe the instability evolution at late times. Figure 4(b) shows the experimental radiographs obtained at t = 39 and 65 ns after the drive beams (shock propagation direction is upward). Growth of the perturbation at the Cu-CH interface is clearly seen as the three black spikes (Cu) interpenetrating the bubbles of polyimide at the bottom of each image. A partial fourth Cu spike is also visible at the left of the image. This spike is highly distorted due to the presence of large vortices at the wall of the tube. Such wall vortices, generated by the interaction of reflected waves and boundary layers at the wall, are also observed in conventional gas-dynamic shock tubes as is discussed in Brouillette and Bonnaza[48]. The dark region located above the Cu spikes is the brominated CH layer. An imprinted perturbation of opposite phase is clearly seen at the interface between this layer and the shocked foam. The separation between the two interfaces was deliberately designed to

generate this phase reversal of the imprinted perturbation in order to distinguish it from any possible imprinting that might arise from the growth of structure at the first interface. At t = 65 ns, the instability at both interfaces has continued to evolve, much of the growth of the Cu-CH interface being due to the rarefaction wave reflected from the second interface.

The results from 2D numerical simulations using both CALE and PROMETHEUS are shown at the same times as the experimental images. The agreement with both codes is seen to be excellent. The magnitude, phase, and shape of the imprinted structure at the second interface are all very similar at both times. There is a small difference in the fourth distorted Cu spike as the wall vortex in the experimental image is somewhat larger than in either simulation. Small differences can also be observed between the two codes concerning secondary structure on both the Cu spikes and the roll-up of CH(Br) at the second interface at 65 ns. The resolution of the data at this scale is insufficient to provide a comparison with the simulations. As with the previous experiment, we conclude that both codes do a very good job of simulating the phenomenon of shock imprinting.

While this experiment is useful for benchmarking code performance, it differs in one important regard from the SN problem. The possibility of imprinting by a rippled shock depends very strongly on the density profile through which the shock propagates. In our experiment, the shock propagated through constant density material before impacting the second interface. As is well known, planar shock propagation in constant density material is stable[49-50]. In the star, by contrast, the decreasing radial density profile can cause portions of the shock located radially further from the center to propagate faster than regions located closer to the center. Thus, shocks can be unstable in a decreasing density profile. This problem has been analyzed by Chevalier[51-52] for an exponentially decaying density profile and by Sari et al.[53] for power law profiles $\rho \sim r^{-\omega}$, where $w > 3$. In both cases, shock instability was shown to be possible for perturbations whose wavelength is much longer than the scale height, overstable for more moderate values of the wavelength, and stable for small wavelengths.

For shock imprinting to occur, we do not require instability of the shock with increasing amplitude as the shock propagates, but merely a small enough decay rate for some perturbation to survive to the second interface. An exact comparison of the possibility of shock coupling in SN 1987A, for example, would require a stability analysis of the spatially varying density profile of that particular progenitor star. From the general form of the analyses of Chevalier et al. and Sari et al., however, it can be concluded that shock imprinting will be most likely to occur for the longest wavelength perturbations. This leads one to consider, as mentioned in the introduction, the possibility of non-symmetrical explosion scenarios with very low mode-number azimuthal perturbations. The jet mechanism of Khokhlov[26] is an extreme case of such a low mode-number perturbation.

C.) The effect of dimensionality (2D vs. 3D)

We turn now to the role of dimensionality in the instability evolution. As mentioned earlier, nearly all simulations to date have been performed in 2D, the only exceptions being refs. [24-25]. It is well known from simple buoyancy-drag models[21] that perturbation growth in three dimensions is greater than in two. The additional mixing arising in a three-dimensional flow would be a likely candidate to explain the SN mixing problem. In order to quantify the contribution of dimensionality, experiments with two equivalent targets have been conducted. Both targets consist of a 108 μm thick layer of 4.3% brominated polystyrene followed by a 1500 μm long cylinder of CRF. The densities of the two materials are the same as used previously. The only difference between the two targets is in the perturbation imposed at the interface as shown in Figure 6(a, b). The 2D target contains a single sinusoidal perturbation of wavelength 50 μm and peak-to-valley amplitude of 5 μm. The 3D target contains a perturbation with two orthogonal sinusoids, both of wavelength 71 μm and overall amplitude 5 μm. The perturbations were chosen such that the wavenumber magnitude is the same for each giving identical RM and RT growth in the linear regime.

Experimental radiographs obtained using 4.7 keV x-rays from a Ti backlighter foil are shown in Figures 6(c) for the 2D target and 6(d) for the 3D target. For both of these targets, no radiographic tracer layer was used, so the images give the integrated differential x-ray absorption through 1500 microns of CH(Br). The target alignment is obviously quite good as the images are looking along 2D ridges 30 times longer than the imposed wavelength of 50 μm. The lack of a radiographic tracer tends to obscure the full extent of the bubbles of the lower density foam, however. From these images, then, we are only able to obtain information concerning the growth of the spikes.

A measure of the difference in growth is obtained from Figures 6(c, d) by comparing the distance between the spike tips and the shock. The relevant dimensions from each experiment are given in the Table below. The average drive energy per beam is within 5% for the two shots. Since ablation pressure goes like $I^{2/3}$, and velocity scales as the square root of the pressure, the difference in interface velocities should be less than 2%. From the measured position of the reference grids, the shock locations in each case are within 10 microns, which is of order of the experimental error. The distance of the spike tips relative to the shock reference is 84 μm for the 2D case and 70 μm for the 3D case, indicating that the 3D spikes have grown approximately 20% more.

2D vs. 3D experiment parameters

Parameter	2D	3D
Drive energy / beam (J)	534.2	505.9
CH(Br) layer thickness (μm)	156	161
Downstream grid position (μm)	791	732
Shock position (μm)	757	767
Spike position (μm)	673	697
Shock-to-spike distance (μm)	84	70

A numerical simulation of this particular experiment has not yet been performed. We can compare with previous numerical studies of similar geometries, however. In Kane et al.[25], for example, the growth of perturbations at the He-H interface of SN1987A was studied using the PROMETHEUS code. Their results also show an increase in the spike growth in 3D over that in 2D, though their increase was approximately 30% as compared with the 20% observed in the present experiments. Their conclusion was that even a 30% increase in the extent of the mixing region was insufficient to explain the observations of SN 1987A.

An improvement in the measurements can be made by again introducing a radiographically opaque tracer strip in the dense material layer as was done in the interface coupling experiment. Figure 6(e) shows the result of that experiment. The perturbation in this case was the same two-dimensional sinusoid as in Figures 6(a & c), and the drive was again nominally the same as that of the other shots. The more narrowly defined region contributing to the radiographic contrast now allows for the visualization of the full extent of the bubbles as well as the spikes. A future series of experiments is planned using this technique to measure the temporal development of the full extent of the mixing layer for both 2D and 3D interface.

D.) The effect of modal content (2-mode experiment)

A final experiment was conducted to begin to explore the evolution of a more complicated interfacial structure. Thus far, we have only investigated single mode interface perturbations. In the SN mixing problem, however, the interface is almost certain to be fully turbulent. A first step toward such an interface structure is to introduce two modes, which through non-linear mode coupling will then begin to generate additional modes in the spectrum, eventually producing a fully turbulent flow.

The configuration for this experiment is very similar to that just described for the previous 2D experiment with the radiographic tracer layer. The only difference was in the

interface perturbation. Two sinusoidal modes with wavelengths of $\lambda_1 = 60$ μm and $\lambda_2 = 40$ μm with initial amplitudes of 1.5 and 1.0 μm, respectively, were machined onto the interface. Figure 7(a) shows an illustration of the machined surface. A lineout through the surface is given in Figure 7(b). The experimental radiographs obtained using 4.7 keV x-rays from a Ti backlighter are shown in Figures 7 (c & d) for t = 13 ns and 26 ns, respectively. The corresponding CALE simulations at the same times are shown below in Figures 7(e & f). The interface structure is considerably more complicated than for the single mode perturbation. Structure is very evident at a wavelength of 120 μm, which is generated from the non-linear interaction of k_1-k_2 modal components.

The agreement between the experiment and the CALE simulation at t = 13 ns is very good, with the exception of the forward shock position which is about 50 μm ahead in the CALE simulation. At t = 26 ns, the shock continues to move too fast and is just off to the right of the image. The structure of the interface is quite similar between experiment and simulation, with the exception of the small vortical structure at the right edge of the largest spikes. This is not seen in the data, though the quality of the experimental image is not really sufficient to make a clear determination. Future experiments of this type will be directed toward the continued evolution of the interface spectrum. Higher spatial magnification and improved experimental resolution will begin to allow us to make more quantitative comparisons with numerical simulations at the level of detail necessary to differentiate between the results of different codes.

V. CONCLUSION

We have reported the results from a wide series of scaled laser experiments designed to test the validity of numerical codes used for the simulation of astrophysical phenomena such as supernova explosions. The need for such a validation stems from the rather long-standing discrepancy between observations and numerical simulation of SN 1987A. The experiments conducted thus far serve two purposes. They have helped to

establish the range of astrophysical phenomena that can be addressed on a laser facility. Problems involving spherical divergence, multiple interfaces, three-dimensional and multi-mode interfaces could be studied in conventional gas-dynamic shock tubes, but not at the strong shock conditions of interest to astrophysics.

These experiments also serve as a first rough assessment of the validity of numerical codes used for astrophysics. To the level and resolution probed thus far, we find the result of numerical simulation to be in general agreement with the experiments. With improvement in the magnification and spatial resolution that have been recently demonstrated on laser experiments[54], we expect to be able to improve these results to the point that we can begin to differentiate between the results of different codes.

Having established a capability for performing relevant scaled experiments in the strong shock regime of interest, we can now begin to extend the range of problems and physics that can be addressed. The recent work of Khokhlov, for example, suggests that the supernova mixing problem may be far from spherical, with strong polar jets and Mach disks accelerating the inner layers to velocities high enough to explain the observations. Having established that we can perform relatively clean spherically divergent experiments, one can now begin to alter the experimental geometry to address the physics introduced by aspherical explosions. We hope to be able to use this testbed to continue to address new ideas as they are introduced in the astrophysical community and to provide benchmark data to augment observation, theory, and numerical modeling.

VI. ACKNOWLEDGEMENTS

Work performed under the auspices of the U.S. Department of Energy Lawrence Livermore National Laboratory under Contract No. W-7405-ENG48.

REFERENCES

[1]Lord Rayleigh, Scientific Papers II (Cambridge, England), p.200 (1900).

[2]G.I. Taylor, *Proc. Roy. Soc. London*, A **201**, 192 (1950).

[3]R.D. Richtmyer, *Commun. Pure Appl. Math.* **13**, 297 (1960).

[4]E.E. Meshkov, *Izv. Acad. Sci. USS Fluid Dynamics* **4**, 101 (1969).

[5]M. Itoh et al., *Nature* **330**, 233 (1987).

[6]W.D. Arnett, J.N Bahcall, R.P. Kershner, & S.E. Woolsey, *Ann. Rev. Astron. Astrophys.*, **27**, 629 (1989).

[7]R.A. Chevalier, *Nature*, **355**, 691 (1992).

[8]F.C. Witteborn, J.D. Bregman, D.H. Wooden, P.A. Pinto, D.M. Rank, S.E. Woosley, & M. Cohen, *Ap. J.* **338**, L9 (1989).

[9]J. Tueller, S. Barthelmy, N. Gehrels, B.J. Teegarden, M. Leventhal, & C.J. MacCallum, *Ap. J.* **351**, L41 (1990).

[10]R. McCray, *ARA & A* **31**, 175 (1993).

[11]I. Hachisu, T. Matsuda, K. Nomoto, & T. Shigeyama, *Ap. J. Lett*, **368**, L27 (1991).

[12]M. Herant & W. Benz, *ApJ*, **370**, L81 (1991).

[13]B.A. Fryxell, E. Muller, & D. Arnett, *ApJ*, **367**, 619 (1991).

[14]E. Muller, E., B. Fryxell, & D. Arnett, *A&A*, **251**, 505 (1991).

[15]R.A. Chevalier, J.M. Blondin, & R.T. Emmering, *Ap. J.* **392**, 118 (1992).

[16]K. Kifonidis, T. Plewa, H.-Th. Janka, & E. Muller, *ApJ*, **531**, L123 (2000).

[17]G. Bazan & W.D. Arnett, *ApJ*, **433**, L41 (1994).

[18]G. Bazan & W.D. Arnett, *ApJ*, **496**, 316 (1998).

[19]W.D. Arnett, *Ann. N.Y. Acad. Sci.*, **898**, 77 (2000).

[20]J.P. Dahlburg, J.H. Gardner, G.D. Doolen, & S.W. Haan, *Phys. Fluids B*, **5**, 571 (1993).

[21]J. Hecht, U. Alon, & D. Shvarts, *Phys. Fluids*, **6**, 4019 (1994).

[22]M. Marinak et al., *Phys. Rev. Lett.*, **75**, 3677 (1995).

[23]T. Yabe, H. Hoshino, & T. Tsuchiya, *Phys. Rev. A*, **44**, 2756 (1991).

[24]M. Herant & W. Benz, *Ap. J.*, **387**, 294 (1992).

[25]J. Kane, J., D. Arnett,, et al., *Ap. J.*, **528**, 989 (2000).

[26]A.M. Khokhlov, P.F. Hoflich, E.S. Oran, J.C. Wheeler, & L. Wang, *ApJ Lett.*, **524**, L107 (1999).

[27]J.J. Quirk, *Int. J. Numer. Methods Fluids*, **18**, 555 (1994).

[28]R.L. Holmes, G. Dimonte et al., *J. Fluid Mech.* **389**, 55 (1999).

[29]B.A. Remington, J. Kane, et al., *Phys. Plasmas*, **4**, 1994 (1997).

[30]R.P. Drake, *J. Geophys. Res.*, **104**, 14 (1999).

[31]J. Kane, J., D. Arnett, et al., *Physics of Plasmas*, **6**, 2065 (1999).

[32]R.A. Remington, R.P. Drake, D. Arnett, & H. Takabe, *Science*, **284**, 1488 (1999).

[33]B.A. Remington, R.P. Drake, D. Arnett, & H. Takabe, *Phys. Plasmas*, **7**, in press (2000).

[34]J.W. Connor & J.B. Taylor, *Nucl. Fusion*, **17**, 1067 (1977).

[35]D.D. Ryutov, R.P. Drake, et al., *Ap. J.*, **518**, 821 (1999).

[36]J.T. Larsen & S.M. Lane, *J. Quant. Spectrosc. Radiat. Transfer*, **51**, 179 (1994).

[37]S.I. Braginski, *Reviews of Plasma Physics*. New York, Consultants Bureau. (1965).

[38]Y.T. Lee & R.M. More, *Phys. Fluids*, **27**, 1273 (1984).

[39]J.G. Clerouin, M.H. Cherfi, & G. Zerah, *Europhys. Lett.*, **42**, 37 (1998).

[40]T.R. Boehly, R.S. Craxton, et al., *Rev. Sci. Intsr.*, **66**, 508 (1995).

[41]J.M. Soures, R.L. McCrory, et al., *Phys. Plasmas*, **3**, 2108 (1996).

[42]T.R. Boehly, D.L. Brown, et al., *Optics-Communications*, **133**, 495 (1997).

[43]D.K. Bradley, J.A. Delettrez, et al., *Phys. Plasmas*, **5**, 1870 (1998).

[44]K.S. Budil, T.S. Perry, et al., *Rev. Sci. Inst.*, **67**, 485 (1996).

[45]R.T. Barton, The CALE computer code, *Numerical Astrophysics*. Boston, Jones and Bartlett, 482 (1985).

[46]R.P. Drake et al., *ApJ*, in submission (2000).

[47]J. Kane et al., *Phys. Rev. Lett.*, in submission (2000).

[48]M. Brouillette & R. Bonazza, *Phys. Fluids*, **11**(5), 1127 (1999).

[49]N.C. Freeman, *Proc. Roy. Soc. London A*, **228**, 341 (1955).

[50]J.J. Erpenbeck, *Phys. Fluids*, **5**(10), 1181 (1962).

[51]R.A. Chevalier, *ApJ*, **359**, 463 (1990).

[52]Luo & R.A. Chevalier, *ApJ*, **435**, 815 (1994).

[53]R. Sari, E. Waxman, & C. Shvarts, *Ap. J. Suppl.*, **127**, 475 (2000).

[54]O. Landen et al., submitted to Rev. Sci. Instr., (2000).

TABLES

Parameter	Supernova	Omega Experiment
Length scale (cm)	9×10^{10}	0.0023
Velocity (km/s)	2000	14
Density (g/cm^3)	0.0075	0.4
Pressure ($dynes/cm^2$)	3.5×10^{13}	1.5×10^{11}
Temperature (eV)	900	2
Z_i	2.0	0.5
A	4.0	8.7
Density of nuclei (cm^{-3})	1.1×10^{21}	2.8×10^{22}

Table I. Fundamental hydrodynamic parameters

Derived parameter	Supernova	Omega Experiment
$v / (p/\rho)^{1/2}$	2.2	2.3
Collisional mfp (cm)	3.6×10^{-3}	4.0×10^{-9}
Kinematic viscosity (cm^2/s)	7.0×10^{7}	0.02
Reynolds number	1.9×10^{11}	1.4×10^{5}
Thermal diffusivity (cm^2/s)	1.2×10^{6}	0.55
Peclet number	1.1×10^{13}	5.9×10^{3}
Radiation mfp (cm)	6.8×10^{2}	2.0×10^{-6}
Radiation Peclet number	1.6×10^{16}	1.6×10^{10}

Table II. Derived parameters

FIGURE CAPTIONS

Figure 1(a) Comparison of the SN He-H interface velocity with the corresponding scaled laboratory experiment.

Figure 1(b) Comparison of the spatial structure of the density and pressure fields of the SN He-H interface and the corresponding CH(Ge)-CRF interface of the scaled laboratory experiment.

Figure 2. 3D CAD drawing of the experimental configuration showing the target package and x-ray backlighter foil with the Omega beams used for initiating the strong shock conditions (drive) and diagnosing the experiment (backlighter beams).

Figure 3. (a) Schematic illustration of the divergent experiments, (b) Experimental radiograph at 13 ns of an unperturbed capsule, (c) Experimental radiograph at 13 ns of a perturbed capsule with $\lambda = 70$ μm, $a_{p-v} = 10$ μm, (d) Experimental radiograph at 26 ns of a perturbed capsule, (e) Higher magnification view of perturbed capsule at 13 ns, (f) Higher magnification view of an equivalent planar target with same initial perturbation and drive as (e).

Figure 4. Comparison of peak-to-valley amplitude of interface instability between spherically divergent and planar experiments.

Figure 5. (a) Schematic illustration of the interface coupling experiments, (b) Experimental radiographs at t = 39 and 65 ns, (c) 2D CALE simulated radiograph of the experiment, (d) 2D Prometheus simulated radiograph of the experiment.

Figure 6. Schematic illustration of (a) 2D and (b) 3D interface perturbation, (c) Experimental radiograph of 2D interface at 13 ns, (d) Experimental radiograph of 3D interface at 13 ns, (e) Improved measurement of the full extent of the mixing region using a 200 μm thick radiographic tracer layer.

Figure 7. (a) Schematic illustration of the two-mode interface perturbation, (b) 1D lineout through the interface, (c) Experimental radiograph of the interface at 13 ns, (d) Experimental radiograph of the interface at 26 ns, (e) 2D CALE simulation of the interface at 13 ns, (f) 2D CALE simulation of the interface at 26 ns.

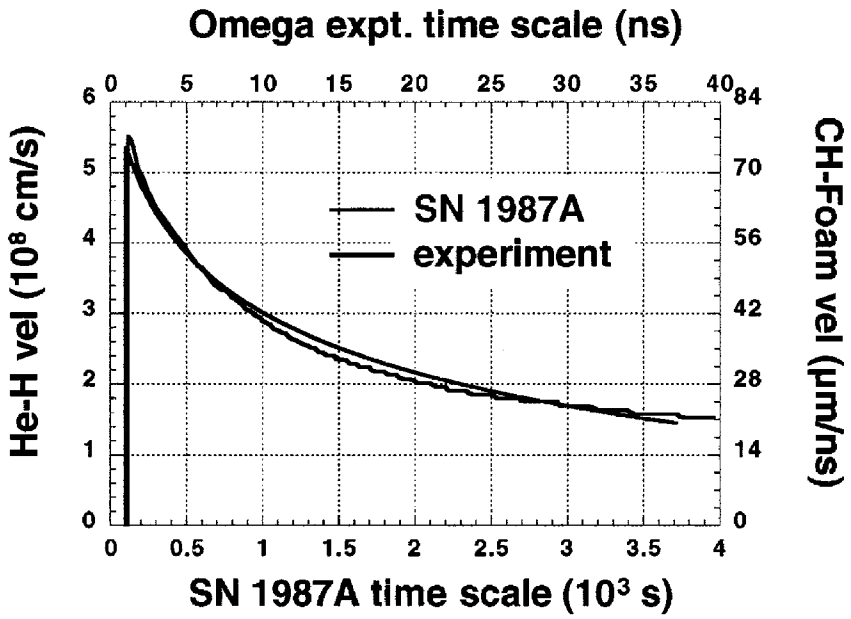

Figure 1(a) Comparison of the SN He-H interface velocity with the corresponding scaled laboratory experiment

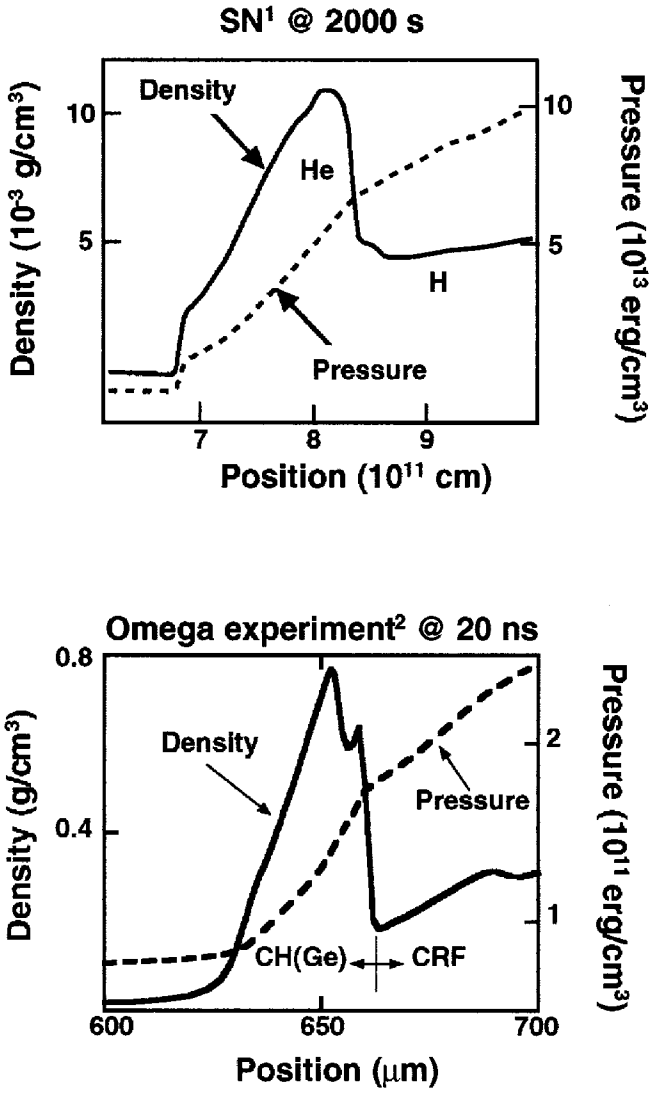

Figure 1(b) Comparison of the spatial structure of the density and pressure fields of the SN He-H interface and the corresponding CH(Ge)-CRF interface of the scaled laboratory experiment

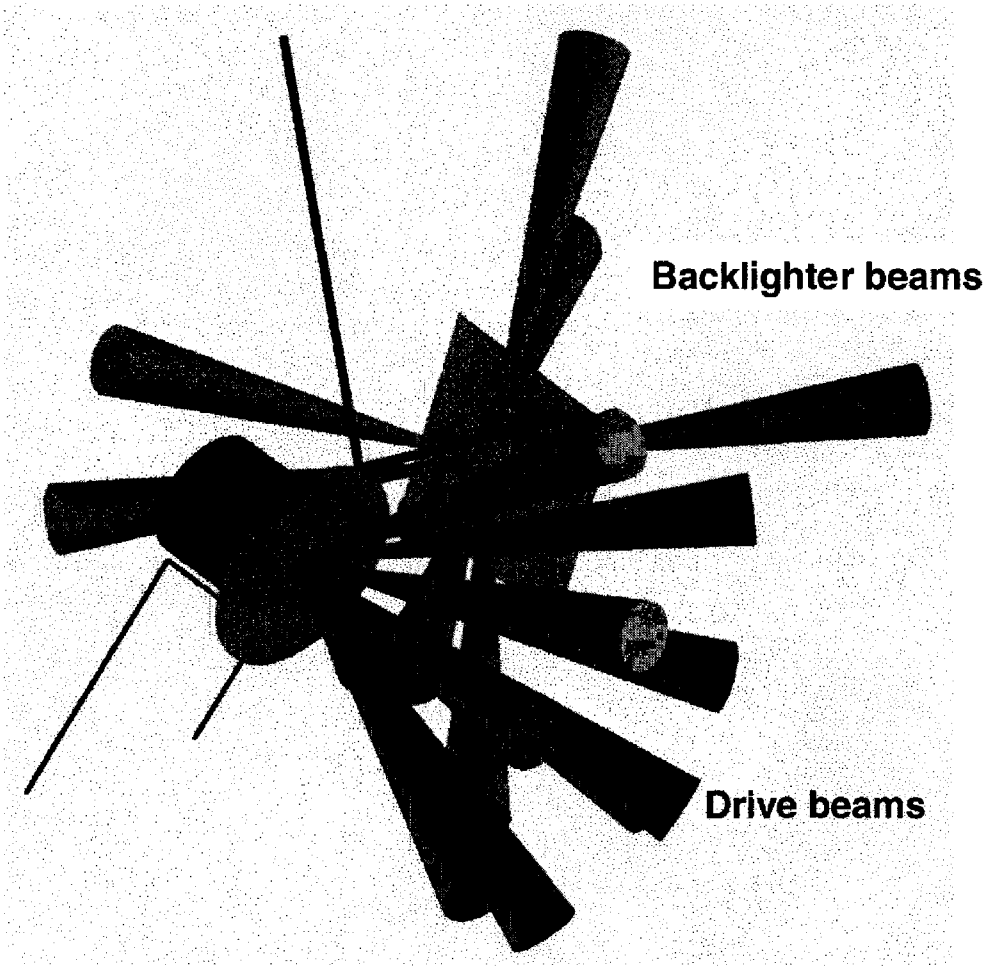

Figure 2. 3D CAD drawing of the experimental configuration showing the target package and x-ray backlighter foil with the Omega beams used for initiating the strong shock conditions (drive) and diagnosing the experiment (backlighter beams).

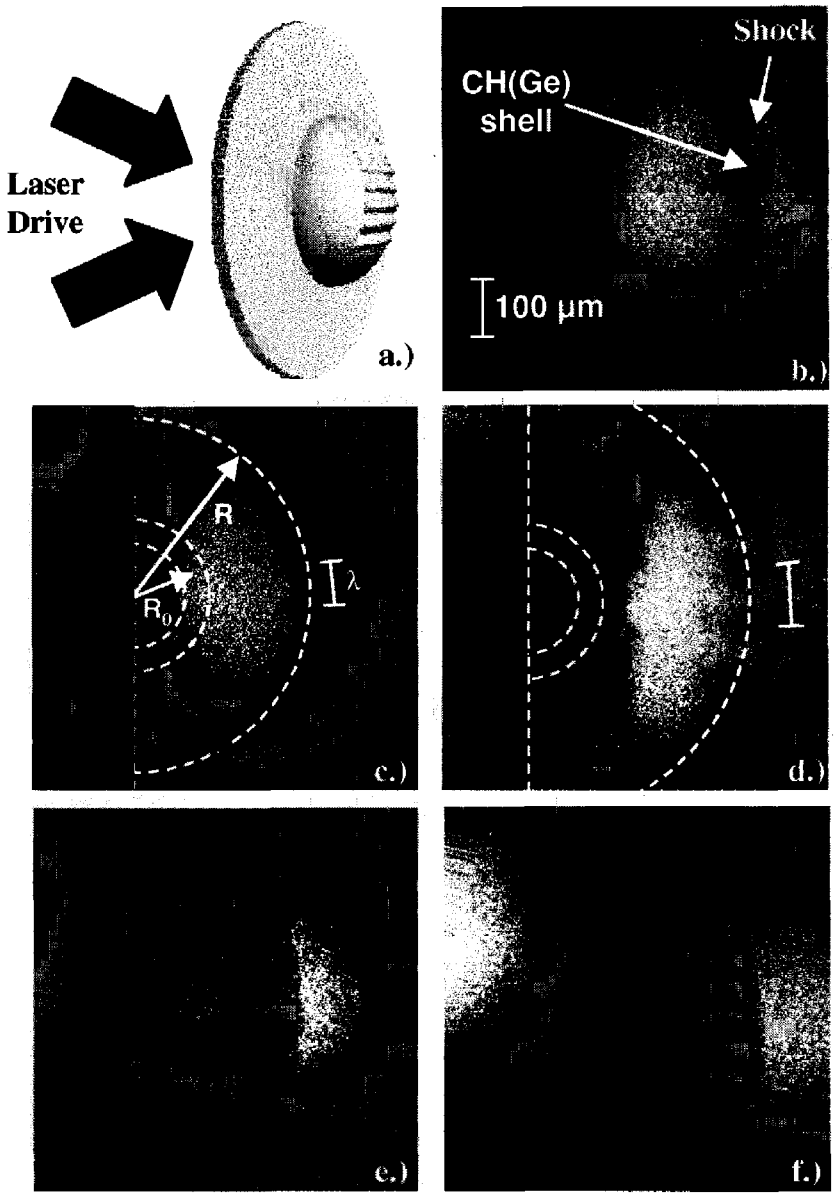

Figure 3. (a) Schematic illustration of the divergent experiments, (b) Experimental radiograph at 13 ns of an unperturbed capsule, (c) Experimental radiograph at 13 ns of a perturbed capsule with $\lambda = 70$ μm, $a_{P-V} = 10$ μm, (d) Experimental radiograph at 26 ns of a perturbed capsule, (e) Higher magnification view of perturbed capsule at 13 ns, (f) Higher magnification view of an equivalent planar target with same initial perturbation and drive as (e).

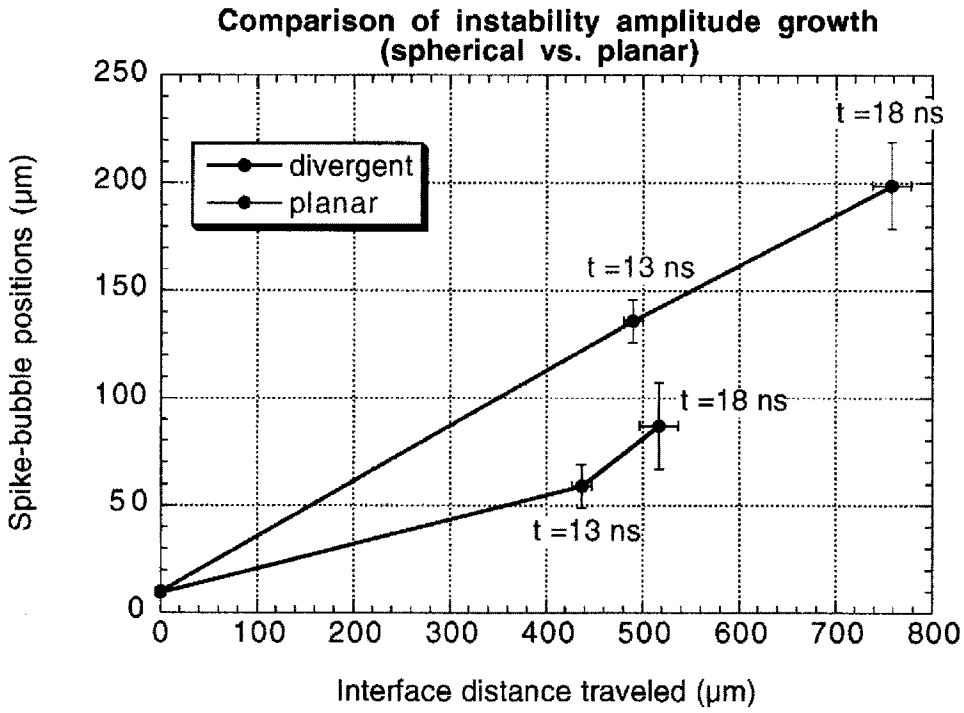

Figure 4. Comparison of peak-to-valley amplitude of interface instability between spherically divergent and planar experiments.

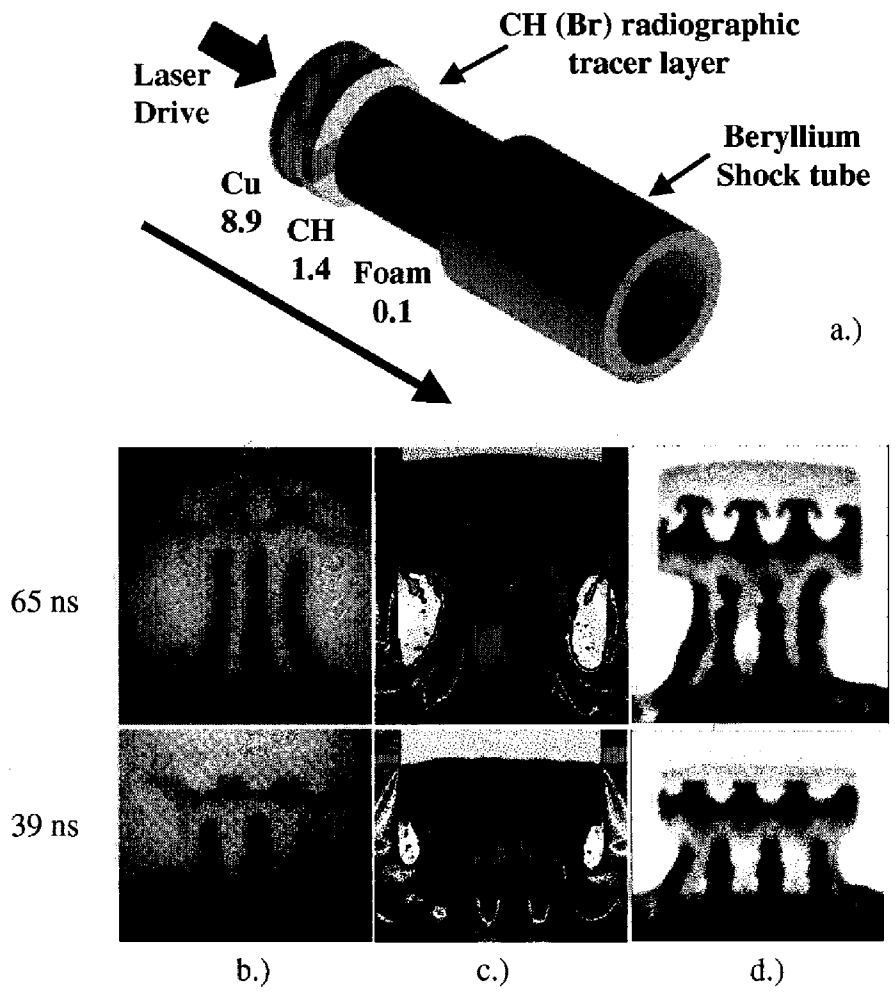

Figure 5. (a) Schematic illustration of the interface coupling experiments, (b) Experimental radiographs at t = 39 and 65 ns, (c) 2D CALE simulated radiograph of the experiment, (d) 2D Prometheus simulated radiograph of the experiment

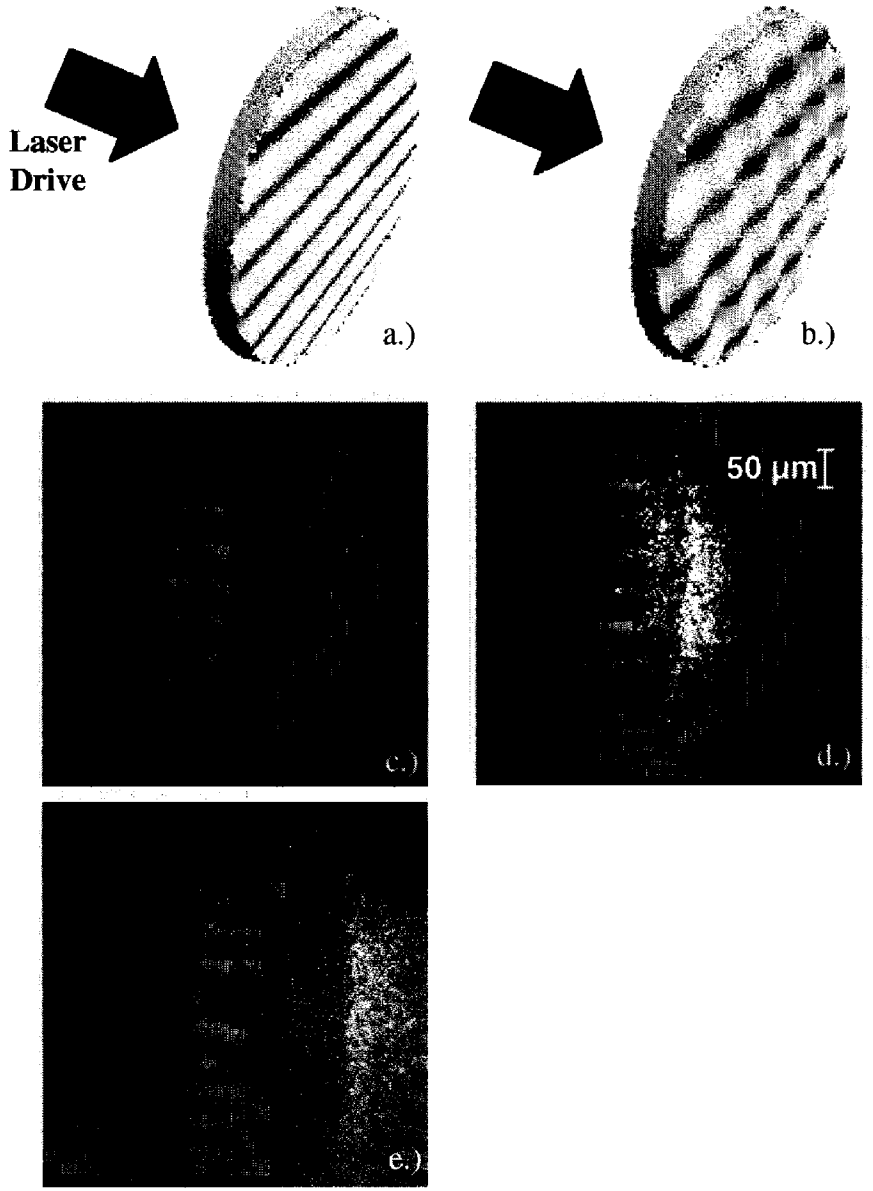

Figure 6. Schematic illustration of (a) 2D and (b) 3D interface perturbation, (c) Experimental radiograph of 2D interface at 13 ns, (d) Experimental radiograph of 3D interface at 13 ns, (e) Improved measurement of the full extent of the mixing region using a 200 μm thick radiographic tracer layer.

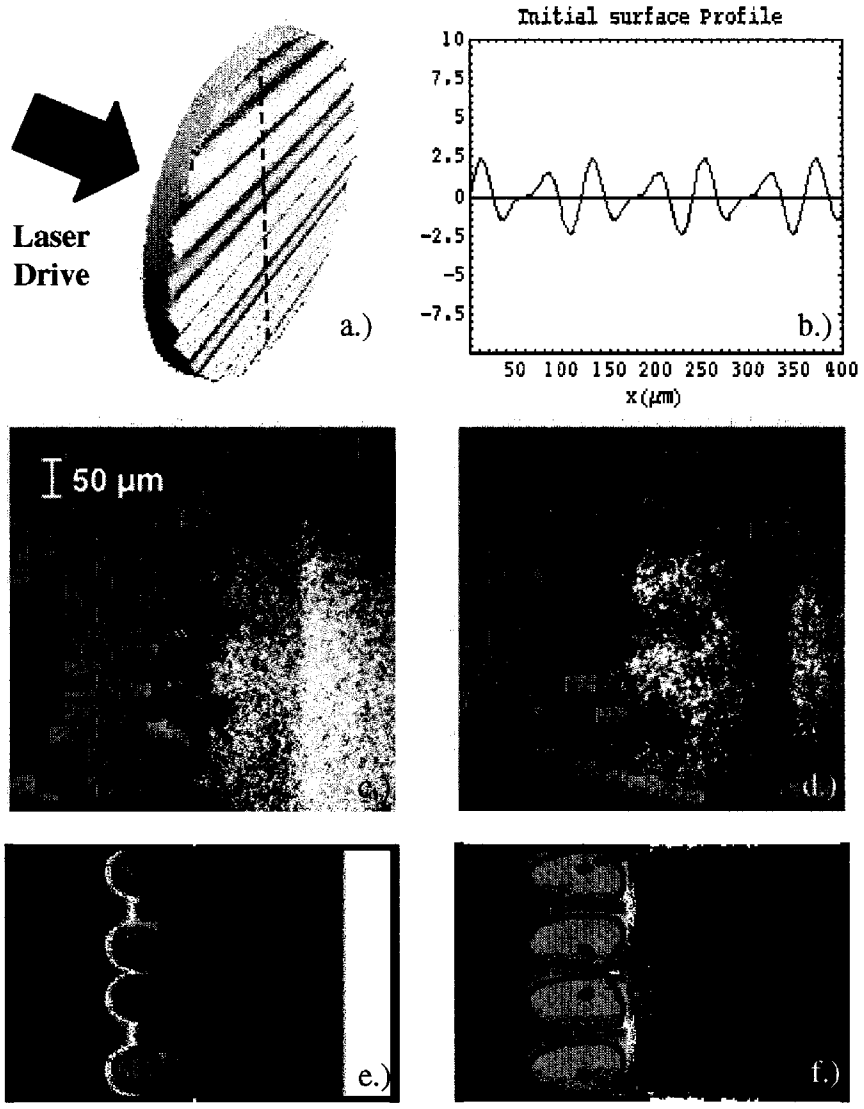

Figure 7. (a) Schematic illustration of the two-mode interface perturbation, (b) 1D lineout through the interface, (c) Experimental radiograph of the interface at 13 ns, (d) Experimental radiograph of the interface at 26 ns, (e) 2D CALE simulation of the interface at 13 ns, (f) 2D CALE simulation of the interface at 26 ns.